Physics of Fluids ARTICLE scitation.org/journal/phf

Turbulent wakes in a non-uniformly stratified environment

Cite as: Phys. Fluids **34**, 105123 (2022); doi: 10.1063/5.0108064
Submitted: 7 July 2022 · Accepted: 17 September 2022 ·
Published Online: 18 October 2022

E. Nadaf, J. M. Brown,[a] and T. Radko

AFFILIATIONS

Naval Postgraduate School, Monterey, California 93940, USA

[a]Author to whom correspondence should be addressed: jmbrown2@nps.edu

ABSTRACT

This study explores the behavior of turbulent wakes generated by a sphere propagating with constant speed in a non-uniformly stratified fluid. The investigation is based on a series of high-resolution direct numerical simulations in which the background stratification is systematically varied. We consider one linear and three nonlinear density profiles and discover that even modest, spatially localized non-uniformities of stratification can profoundly influence the wake dynamics, structure, and evolution. The analysis of microstructure signatures shows that wakes in non-uniformly stratified fluids tend to be more spread horizontally, and internal waves are much stronger than in linear stratification. Simulations performed with Gaussian perturbations are characterized by a vertically asymmetric energy distribution, which is attributed to internal wave reflections from low-gradient regions. Using microstructure decay rates, we estimate the effective persistence period of wakes, showing that it substantially increases with the increasing Froude number. We also find that wakes persist much longer in high-gradient profiles, whereas weak local gradients can substantially reduce the wake longevity.

Published by AIP Publishing. https://doi.org/10.1063/5.0108064

I. INTRODUCTION

Theory of stratified turbulent wakes remains an active research area with applications in nautical and aeronautical engineering, geophysics, and marine biology (Rowe *et al.*, 2020; Snyder *et al.*, 2013; Katija, 2012; Switzer and Proctor, 2000). The wake studies are motivated by the interest in improving the efficiency and control of man-made submersibles (Radko and Lewis, 2019; Spedding *et al.*, 1996) and understanding the predator–prey tracking in biological systems (Wieskotten *et al.*, 2010; Miersch *et al.*, 2011). Stratified wakes have been studied using laboratory experiments (e.g., Schooley and Stewart, 1963; Lin *et al.*, 1992; Meunier and Spedding, 2004; Voropayev *et al.*, 2007), simulations (Gourlay *et al.*, 2001; Brucker and Sarkar, 2010; Diamessis *et al.*, 2011; Moody *et al.*, 2017; Chongsiripinyo *et al.*, 2017, Pal *et al.*, 2017), and analytical models (Meunier *et al.*, 2006; Negretti *et al.* 2006). However, most of such studies focus on the dynamics of wakes in a uniformly stratified environment, which is rarely realized in nature, particularly in the oceanographic context. Some studies have addressed non-uniform stratification in other forms of turbulence, such as studies of Kelvin–Helmholtz instability by Pham *et al.* (2009), Watanabe *et al.* (2018), VanDine *et al.* (2021), and Lewin and Caulfield (2021). In the numerical studies of Pham *et al.* (2009), Watanabe *et al.* (2018), VanDine *et al.* (2021), Kelvin–Helmholtz instability is introduced, which generates a well-mixed region within a uniformly stratified fluid. These studies show that the internal waves carry substantial energy away from the flow even though the local region of the turbulence is well mixed. In particular, Kaminski and Smyth (2019) demonstrated that the mixing efficiency of shear instability depends strongly on preexisting turbulent structure, and thus, it would be expected to be significant to wake dynamics as well. The present investigation examines the effects of non-uniform stratification on wake dynamics, intensity, and persistence. The analysis is based on a series of numerical experiments in which the wake is generated by a solid sphere horizontally propagating through a stratified fluid.

The characteristics of stratified wakes are often described in terms of their dependence on the Reynolds number (Re) and Froude number (Fr) of the flow. The Reynolds number describes the relative importance of advective and viscous forcing and is defined as

$$\mathrm{Re} = \frac{U^* D^*}{\nu^*}, \tag{1}$$

where U^* is the velocity of the body, D^* is the diameter of the body, and ν^* is the kinematic viscosity of the fluid. The asterisks hereafter denote dimensional quantities. At low Reynolds numbers ($\mathrm{Re} \lesssim 2 \times 10^3$), the flow is laminar, and no turbulent mixing is present, but at higher Reynolds numbers ($\mathrm{Re} \gtrsim 4 \times 10^3$), the wake develops turbulence. In both regimes, relatively large-scale vortex streets can also be created along the trajectory of the body (Pao *et al.*, 1982).

The relationship between the advective and buoyancy forces is described by the Froude number

$$\mathrm{Fr} = \frac{U^*}{N^* D^*}, \tag{2}$$

where N^* is the Brunt–Väisälä frequency, the characteristic frequency for internal waves. The Brunt–Väisälä frequency in incompressible fluids is defined as

$$N^* = \sqrt{\frac{-g^*}{\rho_0^*}\frac{\partial \rho^*}{\partial z^*}}, \tag{3}$$

where g^*, ρ_0^*, and ρ^* are the gravitational acceleration, reference density, and density, respectively. As the Froude number increases, it takes longer for the wake turbulence to experience the effects of stratification.

The evolution of stratified wakes has been traditionally separated into three distinct phases: the 3D or near wake, the non-equilibrium or intermediate wake, and the quasi-two-dimensional or late wake (Spedding, 1997). The near wake occurs at early times after the object passage, before the effects of stratification become significant. This phase is characterized by the uniform growth of turbulent structures in the vertical and horizontal directions. The intermediate wake takes place once the wake has begun to collapse vertically. Internal waves radiate the energy in the turbulent wake core, and the wake core flattens (Pao, 1973). As the smaller structures dissipate and the wake enters the late phase, long-lasting, flattened vortex structures become the predominant features in the wake. These so-called pancake vortices can persist long after the initial passage of the body (Redford *et al.*, 2015), and at such late times, the rotation of the Earth can become an important factor (see the discussions from Spedding, 2014; Sutyrin and Radko, 2017; Radko and Lorfeld, 2018). For a detailed description of stratified wake evolution, the authors recommend the reviews by Lin and Pao (1979) and Spedding (2014).

The structure and strength of small-scale turbulence in the wake have been frequently characterized using the turbulent and thermal dissipation rates (e.g., de Stadler, 2013; Redford *et al.*, 2015). These quantities serve as a useful metric for the presence of microstructure—processes operating on the scales of molecular dissipation. The trail of microstructure behind the moving object may be used for wake detection and tracking (Radko and Lewis, 2019). The turbulent and thermal dissipation rates (ε and χ) are readily accessible from the direct numerical simulations (DNS), which makes them a suitable diagnostic tool for quantifying wake behavior and morphology. Therefore, the dissipation rates will be extensively analyzed in the present study as well.

Another key component of stratified wakes is the associated internal wave field. Temperature and velocity disturbances could be transmitted from the source location by internal waves. Therefore, a substantial fraction of the wake energy loss could be attributed to the emission of internal waves (Brucker and Sarkar, 2010). In a linearly stratified environment, internal waves are radiated in all directions with a wide range of frequencies from a moving body (Keller and Munk, 1970). As described by Rottman *et al.* (2004), such waves can be generated in two ways: by fluid shifting away from the object as it passes through the medium (lee waves) or through the excitation by turbulent motions in the wake itself (random waves). Lee waves are the dominant form of internal waves for a spherical body moving through a stratified fluid when $\mathrm{Fr} < 4$, and random waves are dominant at larger Fr (Gilreath and Brandtt, 1985; Hopfinger *et al.*, 1991). Abdilghanie and Diamessis (2013) examined near-field internal waves in a simulation of a towed sphere, finding that internal waves can persist until the start of the late wake and that the intensity of these waves depends strongly on Re. Zhou and Diamessis (2016) confirmed this result and showed that the most energetic waves are created in the early intermediate phase. They also discovered that the internal wave intensity gradually reduces until the late stages of wake evolution, when viscosity becomes the major contributor to kinetic energy decay. These analyses have clearly demonstrated the major influence of internal waves on wake evolution. However, to the best of our knowledge, the role of waves in more realistic non-uniform stratification patterns has not been examined yet. Some studies have investigated how internal waves can carry energy from Kelvin–Helmholtz instabilities in uniform stratification, which generate a weakly stratified turbulent region surrounded by stably stratified fluid. Pham *et al.* (2009) showed through numerical simulations that the internal waves produced at the interface between the weakly stratified and strongly regions are of substantial dynamic importance to the development of the turbulence.

In this study, we analyze a series of high-resolution numerical simulations in which the background stratification is systematically varied. We find that local non-uniformities in the ambient temperature profile significantly affect the dynamics and duration of wakes. In particular, stratification anomalies cause vertical asymmetries in the radiation of internal waves as well as changes in the microstructure signatures and the overall wake pattern. One of the critical mechanisms of wake control is wave related: regions of weak stratification inhibit the transmission of internal waves, which causes their deflection of internal waves away from such areas, which, in turn, affects the distribution of energy and microstructure. We demonstrate that the local stratification anomalies can substantially—by as much as a factor of two—affect the lifespan of a wake.

This paper is organized as follows. Section II introduces the numerical methods and describes the simulation architecture. Section III presents the simulation outputs and their diagnostics focused on the microstructure properties and the internal wave dynamics. We conclude with a summary and some final observations in Sec. IV.

II. METHODS

This study is based on a series of numerical simulations in which a sphere moves with constant velocity through a stationary fluid. We adopt the incompressible, one-component Boussinesq model, ignoring planetary rotation and nonlinearities of the equation of state. Thus, the governing equations are as follows:

$$\frac{\partial \mathbf{u}^*}{\partial t^*} + \mathbf{u}^* \cdot \nabla^* \mathbf{u}^* = -\frac{1}{\rho_0^*}\nabla^* p^* + g^* \frac{\rho^* - \rho_0^*}{\rho_0^*}\hat{\mathbf{k}} + \upsilon^* \nabla^{*2}\mathbf{u}^*, \tag{4}$$

$$\frac{\partial T^*}{\partial t^*} + \mathbf{u}^* \cdot \nabla^* T^* = k^* \nabla^{*2} T^*, \tag{5}$$

$$\nabla^* \cdot \mathbf{u}^* = 0, \tag{6}$$

$$\frac{\rho^* - \rho_0^*}{\rho_0^*} = -\alpha_T^* \left(T^* - T_0^*\right), \tag{7}$$

where $\mathbf{u}^* = (u^*, v^*, w^*)$ is the total velocity vector, $\hat{\mathbf{k}}$ is the vertical unit vector, p^* is the pressure, T^* is the sea-water temperature, and T_0^* is a reference temperature, which is set to be the surface temperature. The remaining constants are the thermal expansion coefficient, α_T^*,

the gravitational acceleration, g^*, the kinematic viscosity, υ^*, the thermal diffusivity, k^*, and the reference density, ρ_0^*. We non-dimensionalize the system using the object diameter as the length unit, $[L] = D^*$, and its speed as the velocity unit such that $[t] = [L]/U^*$. The temperature unit is $[T] = T_z^*[L]$, where T_z^* is the constant background temperature gradient, and the pressure unit is $[p] = \rho_0^*[L]^2/[t]^2$. The non-dimensional equations take the form

$$\frac{\partial \mathbf{u}}{\partial t} + \mathbf{u}\cdot\nabla\mathbf{u} = -\nabla p + \mathrm{Fr}^{-2}T\hat{\mathbf{k}} + \mathrm{Re}^{-1}\nabla^2\mathbf{u}, \tag{8}$$

$$\frac{\partial T}{\partial t} + \mathbf{u}\cdot\nabla T = \mathrm{Pr}^{-1}\mathrm{Re}^{-1}\nabla^2 T, \tag{9}$$

$$\nabla\cdot\mathbf{u} = 0, \tag{10}$$

where the Reynolds number and Froude number are defined in Eqs. (1) and (2). The Prandtl number, Pr, is defined as the ratio of the kinematic viscosity to the thermal diffusivity, $\mathrm{Pr} = \upsilon^*/k^*$. As is common in models of turbulent systems (e.g., de Stadler, 2013), the Prandtl number is taken to be 1. Beyond this assumption, no turbulent sub-grid-scale model is used.

The simulations are performed using OpenFOAM v2012, an open-source software package that is based on a finite-volume spatial discretization and provides a variety of fluid modeling solvers (Weller *et al.*, 1998). This model is chosen because of its wake modeling features, such as dynamic meshing. These simulations use an Euler scheme with the PIMPLE algorithm to evolve the equations forward in time (Holzmann, 2019). The simulations use a finite volume discretization of Gaussian integration with second-order central differencing for interpolation between cells.

A. Simulation setup

The computational domain has dimensions of $60 \times 10 \times 12.5$ in x, y, and z, respectively. The solid object travels along the x axis from the point of origin located 5 length units from the top, side, and $-x$ boundaries to $x = 50$. The domain is discretized in terms of two independent meshes, one which simulates the bulk fluid and remains stationary (the outer mesh) and the other which simulates the fluid immediately around the body and moves with it (the inner mesh). The inner mesh has dimensions of $3 \times 3 \times 3$ and is centered on the body. The purpose of splitting the mesh into the outer and inner meshes is to create a composite domain that can resolve fine-scale features near the submerged object while modeling the larger structures of the wake as they develop. The meshes are evolved using the Overset framework (Tisovska, 2019). The resolution of the outer box is 0.1 in x and y but varies in depth. The domain is most finely resolved in the vertical direction from $z = [-2.5, 2.5]$, where the spacing is uniform with $\Delta z = 0.04$. Above and below this region, the spacing increases exponentially to 0.35 on the top and bottom boundaries. The grid spacing of the inner mesh is 0.05 in all directions at the outer edges but decreases to 0.01 at the body boundary. Each simulation has a total of 10 970 968 cells, and the structures of the outer and inner meshes are illustrated in Fig. 1.

The object is embedded in a surrounding medium with a prescribed initial temperature pattern. The top boundary of the domain is impermeable and stress-free. The side boundaries are periodic, and the bottom boundary is open. The submerged body boundary is impermeable and non-slip, and the normal gradient of temperature is set to zero on its surface.

Our investigation is based on two general stratification patterns. The first group assumes the initial vertical temperature profile given by

$$\overline{T}(z) = z + \gamma\exp\left(\frac{-z^2}{\sigma^2}\right), \tag{11}$$

where γ controls the magnitude of local temperature perturbation and σ determines its vertical scale. The simulations based on (11) are used to explore the effects of local curvature in the background profiles. The second group of simulations is based on

$$\overline{T}(z) = z + \beta\tanh\left(\frac{z}{\delta}\right), \tag{12}$$

where β and δ determine the local gradient and size of the perturbed area, respectively. These stratification patterns are presented in Fig. 2.

Eight specific cases are considered, as summarized in Table I. The first simulation, EXP 1A, is based on a linear background profile, providing a reference for subsequent nonlinear simulations. In EXP 2A,

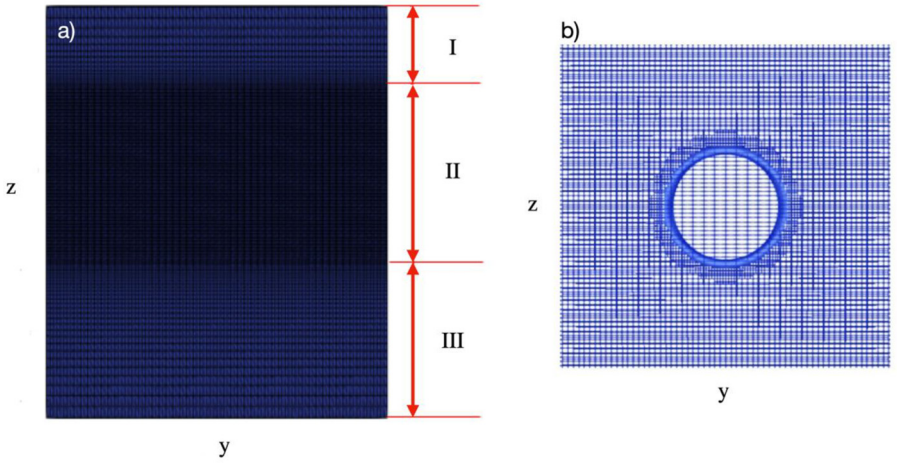

FIG. 1. (a) Vertical section of the outer mesh. From top to bottom: Shallow region (I), intermediate region (II), and deep region (III). (b) Vertical section of the inner mesh.

TABLE I. Summary of all simulations.

Fr = 1.0	γ	β	σ	δ	Fr = 3.2	γ	β	σ	δ	Comments
EXP 1A	0	⋯	⋯	⋯	EXP 1B	0	…	⋯	⋯	Linear stratification
EXP 2A	2	⋯	2	⋯	EXP 2B	2	⋯	2	⋯	Gaussian perturbation
EXP 3A	⋯	1	⋯	0.2	EXP 3B	⋯	1	⋯	0.2	High gradient
EXP 4A	⋯	−1	⋯	1.1	EXP 4B	⋯	−1	⋯	1.1	Low gradient

this linear initial background is modified by adding a Gaussian perturbation (11). Only a positive Gaussian perturbation is considered here since it can be shown (Appendix A) that the solutions for the corresponding positive and negative perturbations are isomorphic. In EXP 3A and EXP 4A, initial stratification is described by Eq. (12). EXP 3A (EXP 4A) has a large (small) local temperature gradient at $z = 0$ but the same gradient in the far-field as EXP 1A. The aforementioned simulations assume Fr = 1, and EXP 1B–EXP 4B represent their counterparts performed with Fr $= \sqrt{10} \approx 3.2$. In all simulations in this study, the Reynolds of the flow is Re = 5000.

B. Verification, validation, and resolution metrics

We verify and validate our results by compared to those of Bonnier and Eiff (2002) and Pal *et al.* (2017). We perform a single simulation for this purpose with Re = 3700 and Fr = 3. These parameters match the values using in a numerical simulation by Pal *et al.* (2017). The laboratory experiment of Bonnier and Eiff (2002) has Re = 6900 and Fr = 3, but it yields comparable results and is also included. We bin our results logarithmically in terms of $N_0 t_s$, where $t_s(x,t) = t - x$ is the non-dimensional time since the passage of the submerged object through a given x-normal plane, and $N_0 = \mathrm{Fr}^{-1}$ is the non-dimensional global buoyancy frequency of the system. This permits the representation of the typical wake behind the object at a certain time. We calculate both the mean streamwise velocity on the axis of travel and the rms value of the same velocity component within each bin. Both quantities are shown in Fig. 3, where they show comparable values to the prior studies. For this simulation, we calculate the Kolmogorov scale $[\eta = (\upsilon^2/(\nabla \mathbf{u})^2)^{1/4}]$ to be above 0.005 within three body diameters and above 0.01 throughout most of the wake. We test the resolution at the body by measuring $y^+ = d\,u_\tau/\nu$, where d is the distance from the object wall, $u_\tau = \sqrt{\upsilon \partial u_{||}/\partial d|_{d=0}}$ is the frictional velocity at the wall, and $u_{||}$ is the velocity parallel to the wall. The extent of the cell closest to the wall ranges from $y^+ = 0.1$ to $y^+ = 0.5$ across the body, which resolves the viscous boundary layer.

III. RESULTS

Figure 4 depicts the typical development of a stratified wake in a uniformly stratified environment with Fr = 1. The turbulent wake begins to form after the passage of the body and then spreads both vertically and horizontally. The disorganized turbulence behind the object is quickly obscured by the development of internal waves, which radiate away from the wake. As the internal waves weaken, the turbulent core of the wake is revealed again near $x = 35$. At this instant, the turbulent wake core is already substantially flattened, which is interpreted as a manifestation of wake collapse. The onset of the near-equilibrium wake is apparent as the flattened wake core is beginning to expand both vertically and horizontally. In this uniformly stratified environment, the turbulent wake and associated internal waves are vertically symmetric, but the introduction of asymmetric perturbations changes this picture substantially.

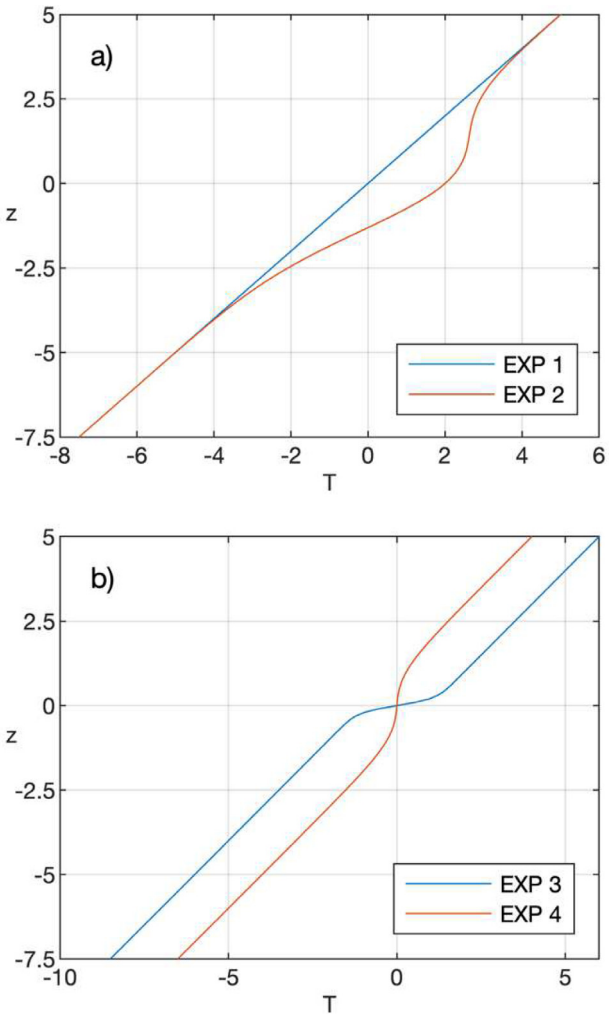

FIG. 2. Characteristic temperature profiles used in the simulations: (a) EXP 1A,B and 2A,B, and (b) EXP 3A,B and 4A,B.

Figure 5 shows typical vertical (a) and (b) and horizontal (c) and (d) cross-sections of the temperature perturbation away from the initial field for EXP 1A and EXP 2A. The internal waves generated by the body are visible and are vertically symmetric around the wake for the linearly stratified simulation. However, they show substantial asymmetry for the Gaussian-perturbed stratification (EXP 2A,B). In addition, the internal waves for EXP 2A are initially more intense than those of the linearly stratified simulation, and this increased intensity remains prevalent long after the initial passage of the body. The horizontal cross-sections in Figs. 4(c) and 4(d) demonstrate the lateral expansion

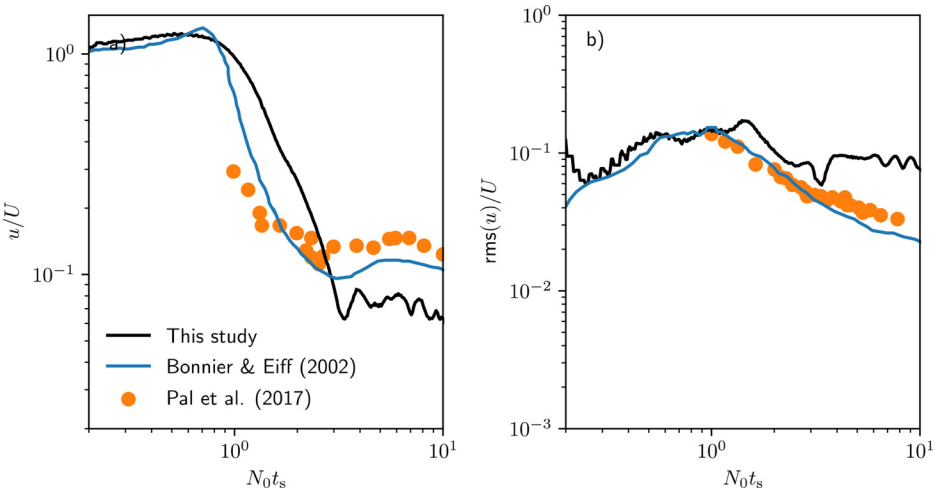

FIG. 3. The centerline velocity of a test problem with $\mathrm{Re} = 3700$ and $\mathrm{Fr} = 3$ compared with the same quantities from Bonnier and Eiff (2002) and Pal *et al.* (2017). The centerline streamwise velocity, binned according to $N_0 t_s$.

of the turbulent wake core. The horizontal extent of the wake for the Gaussian perturbation is greater than for the linearly stratified case even though the local gradients at $z = 0$ are the same in both cases. One possible explanation is that the increased intensity of the internal waves in the Gaussian case leads to a more rapid transfer of the potential energy trapped in the wake core to the surrounding fluid, which permits a quicker collapse of the wake.

A. Microstructure

We quantify the intensity of the wake-induced microstructure using the turbulent and thermal dissipation rates. The dimensional turbulent dissipation rate is defined as

$$\varepsilon^* = \upsilon^* |\nabla^* \mathbf{u}^{*\prime}|^2, \tag{13}$$

where the prime indicates the deviation from a local spatial average. We calculate the local spatial average using a three-dimensional Gaussian window with a variance of 1 to smooth the data. The non-dimensional equivalent of (13) is

$$\varepsilon = \mathrm{Re}^{-1} |\nabla \mathbf{u}'|^2. \tag{14}$$

The thermal dissipation rate is defined as

$$\chi^* = 2k^* |\nabla^* T^{*\prime}|^2, \tag{15}$$

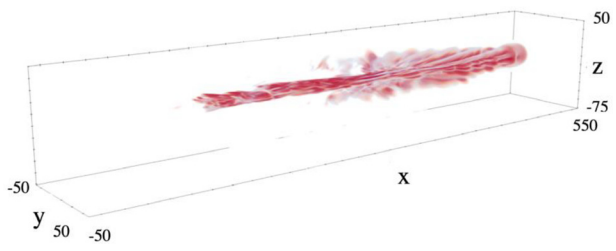

FIG. 4. Wake formation in EXP 1A. The wake core along the object's path and the internal waves being irradiated from the wake can be seen in the gradient of the velocity field ($|\nabla u|$). High values of $|\nabla u|$ are shown in red, moderately low values in blue, and very low gradients are transparent.

and its non-dimensional equivalent is

$$\chi = 2\mathrm{Pr}^{-1}\mathrm{Re}^{-1} |\nabla T'|^2. \tag{16}$$

These quantities are frequently utilized as convenient metrics of small-scale turbulence. The dissipation rates (ε and χ) are often assumed to be proportional to each other, but recent studies have shown that they can vary independently and exhibit dissimilar distribution patterns (Gregg *et al.*, 2018). We restrict our analysis of these quantities to a subset of the domain from $x = 20$ to $x = 30$, which is far from the initial and final positions of the object (where transient wake features are expected).

Figure 6 shows a cross section of χ for the linearly stratified and Gaussian cases at $N_0 t_s \sim 5$, at $x = 25$. The wake is wider for the Gaussian-perturbed cases—which is consistent with the diagnostics in Fig. 5—and at higher values of Fr. This result is expected, as the early wake evolves on a turbulent timescale, which is shorter in terms of $N_0 t_s$ for higher values of Fr, leading to a more rapid initial expansion. The timescale that governs the vertical collapse, however, is controlled by buoyancy. Thus, the vertical extents of the wake are comparable in all simulations at given $N_0 t_s$. Figure 6 also reveals that the internal waves propagate asymmetrically for the Gaussian case and symmetrically for the linearly stratified case, although this effect is substantially more pronounced at lower values of Fr. At this earlier time, the internal waves are largely dominated by regular, radially oriented lee waves. From this perspective, the increased intensity of the internal waves for the Gaussian cases is more apparent (EXP 2A,B), and they are expected to contribute more significantly to wake development.

In Fig. 7, we plot a cross section of χ for the linearly stratified and Gaussian-perturbed simulations at $N_0 t_s = 25$ and $x = 25$. By this time, the turbulent wake core has substantially dissipated, and the internal wave structure is more pronounced. At low values of Fr, the lee waves are still the dominant component of the internal wave field, but at higher values of Fr, the presence of random waves originating from the wake itself is more apparent. In particular, the internal waves propagate asymmetrically in the Gaussian-perturbed cases, favoring transmission through the high buoyancy frequency layer (bottom) of the perturbation.

Figure 8 shows the cross section of χ for EXP 3B and 4B (the case with high and low local gradients, respectively) at $N_0 t_s = 25$ and

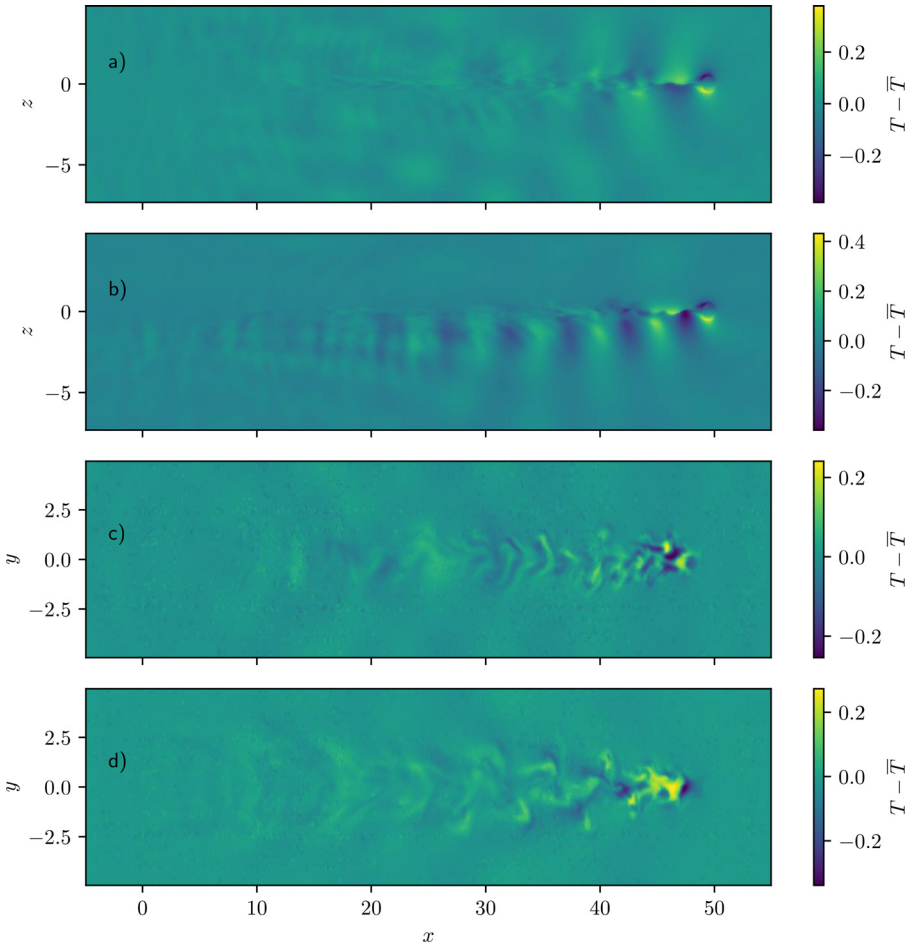

FIG. 5. Comparative analysis of the linearly stratified (EXP 1A) and the Gaussian-perturbation (EXP 2A) simulations. (a) Vertical cross section of T' for EXP 1A. (b) Vertical cross section of T' for EXP 2A. (c) Horizontal cross section of T' for EXP 1A. (d) Horizontal cross section of T' for EXP 2A.

$x = 25$. For reference, the buoyancy frequency profiles are also shown. The simulations with $\mathrm{Fr} = 1$ behave similarly and are not presented here. In the high-gradient case, the increased stratification at the level of the object constrains vertical displacements, and the wake remains confined to the depth of the body. This elevated temperature gradient also results in strong local variations in temperature perturbations, leading to large thermal dissipation. In contrast, the low-gradient case is characterized by wake expansion and low thermal dissipation throughout the low-gradient region ($-3 < z < 3$). The internal waves transmitted in the high local gradient case are weaker than in the linearly stratified simulation but comparable to those in the low-gradient simulation. This result is consistent with a pattern that was apparent in Fig. 7: internal waves can easily propagate from regions of low local buoyancy frequency to high local buoyancy frequency, but the opposite is rare. In particular, EXP 4B shows remarkable similarity to the results of numerical simulations of Kelvin–Helmholtz instabilities in uniform stratification. Pham *et al.* (2009) and Lewin and Caulfield (2021) show that turbulence within a mixed region adjacent to a stratified region results in the generation of internal waves. The properties of these waves are strongly related to the turbulence itself, with some features appearing from large-scale structure and others from random turbulence, analogous to the behavior of lee and random waves in wakes. Pham *et al.* (2009) demonstrate that for internal waves to spread to the stratified region, the Richardson number of the flow [$\mathrm{Ri} = N^2/(\frac{du}{dz})^2$] must be greater than 0.18 in the stratified region. Using the speed of the body and the size of the body to determine a rough shear magnitude (U^*/D^*) gives values of $\mathrm{Ri} = 0.09$ for $\mathrm{Fr} = 1$ and $\mathrm{Ri} = 0.36$ for $\mathrm{Fr} = 3$. Consistent with this, we see little indication of internal waves in Fig. 8.

Figure 9 shows the turbulent dissipation rate (ε) for all simulations in this study at $N_0 t_s \sim 25$ and $x = 25$. Unlike the dissipation rate of thermal variance (χ), the turbulent dissipation rate highlights the behavior of the turbulent wake rather than the internal waves. Thus, ε is more coherent than χ and more concentrated around the trajectory of the wake-generating object. Nevertheless, upward displacements of the wake are evident for simulations with higher Froude numbers. Again, consistent with the findings of Pham *et al.* (2009), the internal wave structure in the stratified regions is much less apparent in the cases with $\mathrm{Fr} = 3$, as the Richardson number is above their threshold.

Figure 10 shows the time evolution of the maxima of χ and ε for all simulations. We define the local maximum for a quantity f as

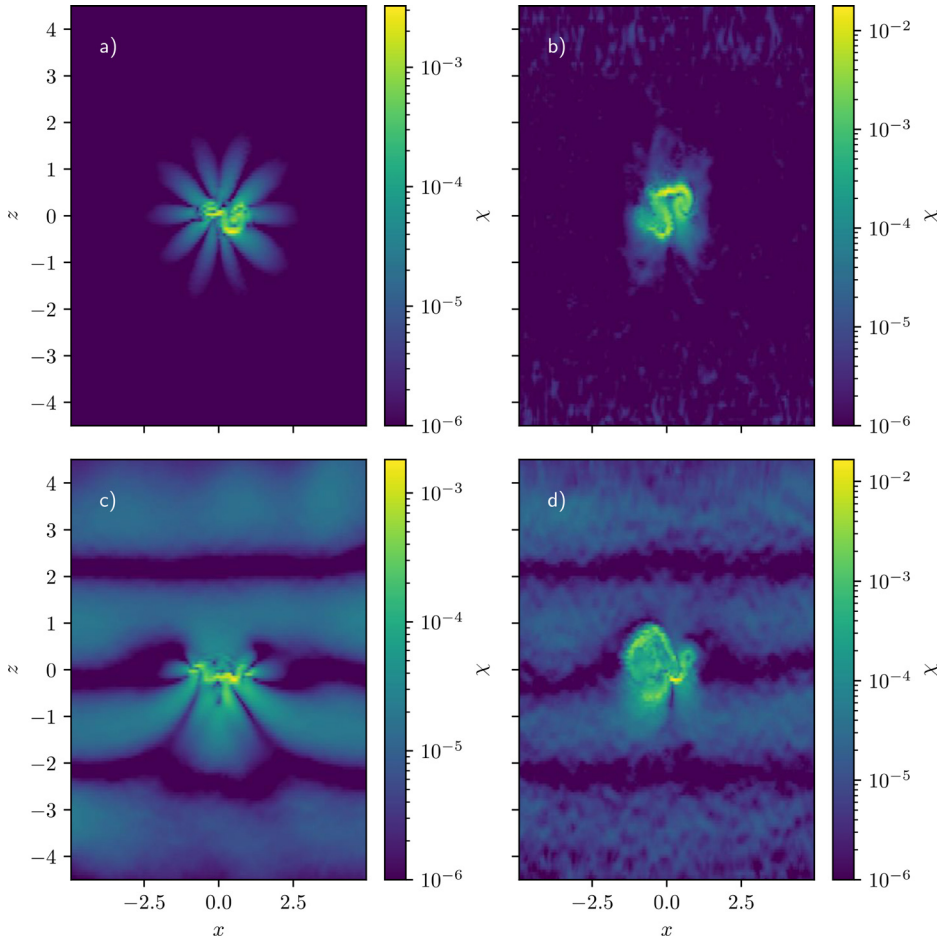

FIG. 6. The y–z cross sections of the thermal variance dissipation (χ) for linearly stratified (EXP 1A,B) and Gaussian-perturbed (EXP 2A,B) systems at $N_0 t_s = 5$: (a) EXP 1A, (b) EXP 2A, (c) EXP 1B, and (d) EXP 2B.

$$f_{\max}(x,t) = \max[f(x,y,z,t)]_{yz}, \tag{17}$$

where the maximum is taken in the y and z directions only. We then bin these results by $N_0 t_s$ and take the mean of each bin. We limit our analysis to regions, where $20 < x < 30$. In Fig. 10, we also show the theoretical minimum detection threshold of $\varepsilon^*_{cr} = 10^{-8}\,\mathrm{W/kg}$ and $\chi^*_{cr} = 10^{-8\circ}\mathrm{C}^2/\mathrm{s}$ (e.g., Waterhouse *et al.*, 2014). We use $D^* = 10\,\mathrm{m}$, $U^* = 5\,\mathrm{m/s}$, and $\frac{\partial T^*}{\partial z^*} = 0.02\,^\circ\mathrm{C/m}$ as nominal scales in converting these instrumental limits to our non-dimensional units. In all cases, the turbulent dissipation attains its maximal value shortly after the passage of the body. As the wake spreads, the turbulent dissipation rate gradually decreases—see the discussion in Radko and Lewis (2019). The mixing induced by the turbulence leads to local changes in the temperature perturbation, causing the thermal dissipation rate to gradually rise until $N_0 t_s \sim 2$, when the effects of buoyancy become more pronounced, and the wake begins to collapse. Eventually, both the thermal and turbulent dissipation rates decay below the detectable levels. The patterns of the turbulent dissipation rate are surprisingly close in all cases, although the decay rate is slightly faster for $\mathrm{Fr} = 3.2$, showing no notable changes with local perturbations in stratification. However, the thermal dissipation rate exhibits substantial variations. Though changes for the Gaussian-perturbed case are limited, the low- and high-gradient cases yield thermal dissipation rates that are more than an order of magnitude below and above the linear case, respectively. The decay timescales are comparable, which indicates that regions with locally elevated stratification could support substantially longer-lasting wakes.

We use these measurements of the maximal turbulent and thermal dissipation to determine the rate of decay and the typical duration of the wake. The decay rate is calculated by fitting ε and χ for each simulation to the following expressions:

$$\varepsilon = C_\varepsilon (N_0 t_s)^{\lambda_\varepsilon}, \tag{18}$$

$$\chi = C_\chi (N_0 t_s)^{\lambda_\chi}, \tag{19}$$

where (C_ε, C_χ) and $(\lambda_\varepsilon, \lambda_\chi)$ are fit parameters. In particular, $(\lambda_\varepsilon, \lambda_\chi)$ represent the decay rates of turbulent and thermal dissipation and are estimated from $N_0 t_s > 1$ and $N_0 t_s > 4$, respectively. These ranges correspond to the intervals of well-defined algebraic decay. We make an exception for EXP 4A—which experiences a substantial delay in reaching the maximum thermal dissipation—and limit our analysis to $N_0 t_s > 10$. The values of λ_ε and λ_χ are shown in Table II for all simulations. The measured turbulent decay rates for all simulations are comparable. In general, they are slightly lower than the prediction of Spedding (1997), who found

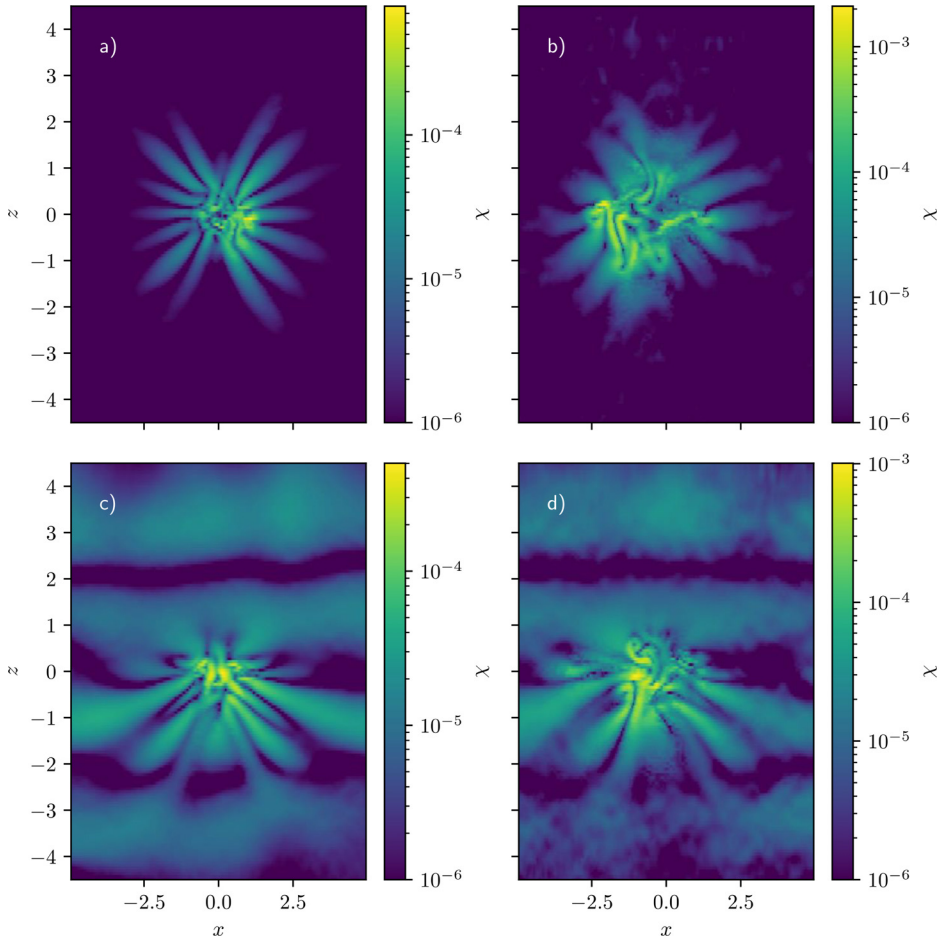

FIG. 7. The y–z cross sections of the thermal variance dissipation (χ) presented in the same manner as in Fig. 6 but for $N_0 t_s \sim 25$: (a) EXP 1A, (b) EXP 2A, (c) EXP 1B, and (d) EXP 2B.

a $-7/3$ power law for stratified wakes at early stages. Comparable to the results of Lewin and Caulfield (2021), we find that the decay of the turbulence itself does not strongly relate to the structure of the stratification. We then use the instrumental threshold $(\varepsilon^*_{cr}, \chi^*_{cr})$ as our diagnostic limit for the wake detectability and solve Eqs. (18) and (19) for the value of t_s at which ε and χ fall below this threshold, which we designate as D_ε and D_χ, respectively. We include these values in Table II. The ε-based signatures typically last between 10 and 30 time units and exhibit very limited sensitivity to the background stratification. However, thermal dissipation shows substantial variation in wake duration. The cases with Fr $= 1$ last up to an order of magnitude longer than those with Fr $= 3.2$. In addition, the perturbations to stratification can result in a factor of two or more difference in the wake duration relative to the linearly stratified simulation. In particular, the high-gradient cases (EXP 3A,B) are characterized by the longest wake duration and the low-gradient cases (EXP 4A,B)—the shortest. We also investigate how the drag coefficient varies with stratification in Table II. The drag coefficient is defined in our non-dimensional units as

$$c_d = \frac{2}{A}\left(\oint p\hat{\mathbf{n}}\cdot\hat{\mathbf{i}}dA + \mathrm{Re}^{-1}\oint \nabla u\cdot\hat{\mathbf{n}}dA\right), \tag{20}$$

where $\hat{\mathbf{n}}$ is the unit vector normal to the surface of the body, $\hat{\mathbf{i}}$ is the unit vector in the x direction, and A is the surface area of the body over which the surface integral is taken. Generally, perturbations in the stratification have negligible effects on the drag coefficient.

B. Internal waves

The non-uniformity of background stratification also profoundly impacts the transmission and reflection of internal waves through the domain. To investigate this, we measure the kinetic energy radiated by internal waves into the regions outside of the wake core in each simulation. We define the kinetic energy above the wake (K_{EA}), and below it (K_{EB}) as

$$K_{EA} = \frac{1}{2}\int\int_{z=3}^{z=5}\int_{x=20}^{x=30}\rho_0(u^2+v^2+w^2)dV, \tag{21}$$

$$K_{EB} = \frac{1}{2}\int\int_{z=-5}^{z=-3}\int_{x=20}^{x=30}\rho_0(u^2+v^2+w^2)dV. \tag{22}$$

The diagnostics are carried out in regions separated by at least 3 units in z from the x axis to exclude the turbulent core of the wake, which makes it possible to focus on principally wave-induced motions. The results are shown in Fig. 11, in which the kinetic energy in the internal

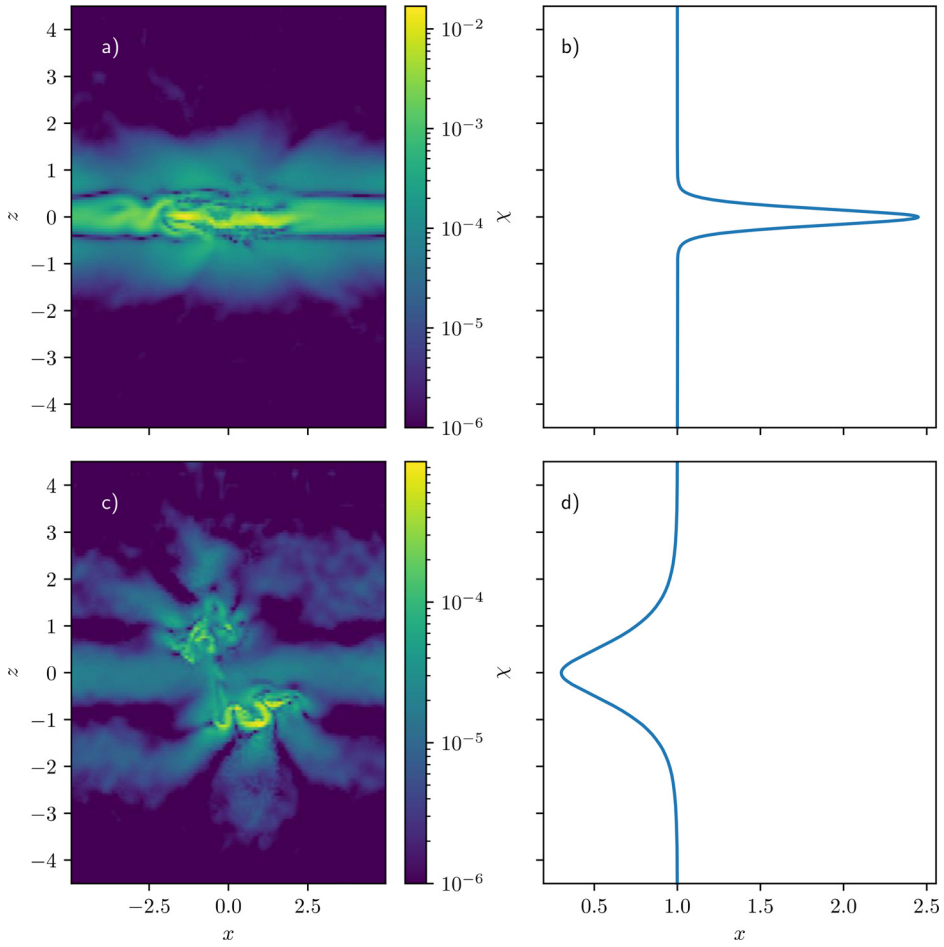

FIG. 8. The y–z cross sections of χ for EXP 3B and EXP 4B at $N_0 t_s = 25$ are shown in (a) and (c), respectively. The panels (b) and (d) present the corresponding initial profiles of the Brunt–Väisäla frequency (N).

waves is plotted in terms of the ratio of K_{EA} to K_{EB}, which is referred to as the ratio of total kinetic energy (RKE). The internal wave energy is distributed symmetrically over the domain for most simulations with $\mathrm{Fr} = 1.0$, although in some simulations with $\mathrm{Fr} = 3.2$, the energy is much more concentrated in the upper region. However, the behavior of the Gaussian-perturbed simulations is highly sensitive to the values of Fr. For $\mathrm{Fr} = 1.0$, the signal above $x = 3$ is very low, suggesting the suppression of internal waves. For $\mathrm{Fr} = 3.2$, internal waves are more prevalent in the upper part of the domain. To understand this phenomenon, we investigate how internal waves are transmitted and reflected.

To do so, we construct a two-dimensional analytic model for the reflection coefficient, R, for a given plane wave. The quantity R is the ratio of the amplitude of the reflected wave (in complex space) to that of the incident wave. For details on the analytic model, see Appendix B. For a given background stratification, this reflection coefficient depends only on the wave vector of the plane wave, $\mathbf{k}$, which also determines the frequency, ω, and angle of propagation from the horizontal, θ. In Fig. 12, we show how this reflection coefficient varies with frequency and horizontal wavenumber for the stratification of EXP 2A, for which the internal wave propagation is most distinct from EXP 1A (for which $R = 0$). In general, there exists a critical frequency above which an incident wave is almost entirely reflected. This is because internal waves can only exist at frequencies between $-N$ and N. When the buoyancy frequency falls below the angular frequency of an internal wave, the wave amplitude exponentially decays. In addition, as the wavelength of the internal wave becomes large with respect to the size of the background perturbation, it becomes more likely that some fraction of the wave will be transmitted even though the region would ordinarily forbid the transmission of the wave (which is expected of evanescent waves).

In our problem, we see that very few of the internal waves produced by the wake in our Gaussian-perturbed simulations transmit through the low buoyancy frequency region above the wake at $\mathrm{Fr} = 1$ but not at $\mathrm{Fr} = 3.2$ (see Fig. 7). This effect is largely due to the inability of the waves to pass this boundary. By construction, the buoyancy frequency at the location of the body is $N_0 = \mathrm{Fr}^{-1}$. Meunier *et al.* (2018) showed that lee waves typically have wavelengths proportional to the Froude number and the diameter of the object ($k_y \sim \mathrm{Fr}^{-1}$). If the lee waves are stationary in the frame of the object, the x-component of the wave velocity is 1, which gives an angular frequency of roughly

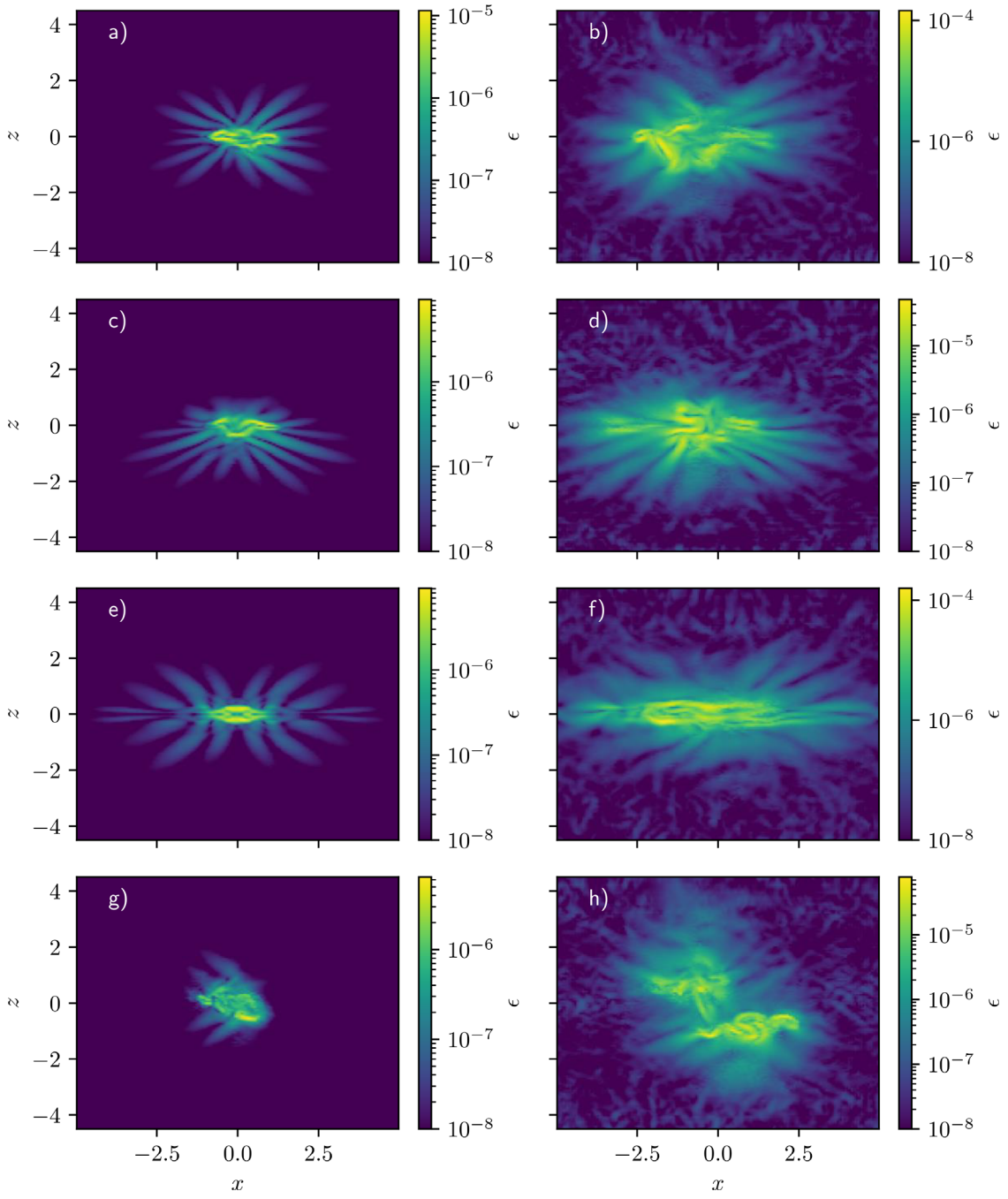

FIG. 9. The y–z cross sections of ε for EXP 1A–EXP 4A at $N_0 t_s = 25$ are shown in (a), (c), (e), and (g), respectively. Panels (b), (d), (f), and (h) show the corresponding patterns for EXP 1B–EXP 4B.

$\omega \sim \mathrm{Fr}^{-1}$ and angles given by $\cos\theta = \omega/N_0 \sim \mathrm{Fr}^0$. Thus, at higher Froude numbers, longer horizontal wavelengths are expected with no effective change in the angle of propagation. Such waves are less likely to be completely blocked by a local minimum in the buoyancy frequency, as shown in Fig. 12.

IV. CONCLUSIONS

We have performed a series of direct numerical simulations of the flow generated by a moving sphere and analyzed the wake sensitivity to changes in both ambient and local stratification. The simulations show that these changes can profoundly affect wake dynamics and intensity.

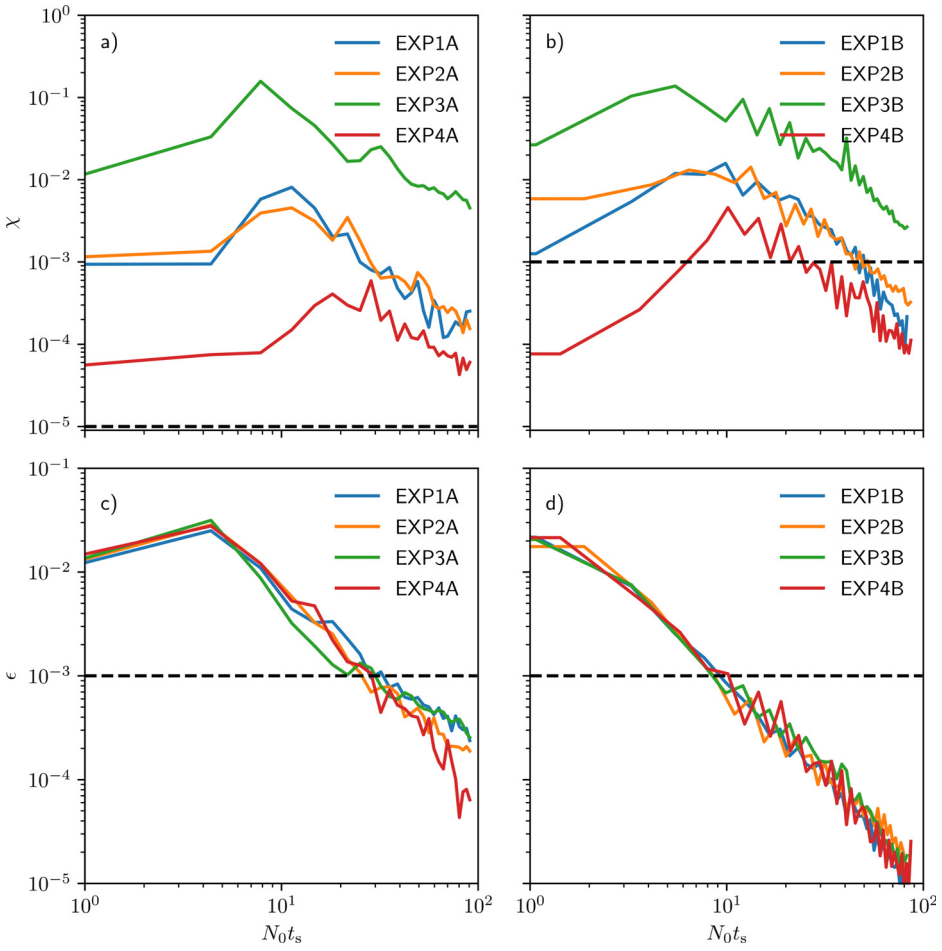

FIG. 10. The maximal dissipation rates of thermal variance, χ, are plotted as a function of time in panels (a) for Fr = 1.0, and (c) for Fr = 3.2. The corresponding records of the turbulent dissipation rate, ε, are shown in panels (b) for Fr = 1.0, and (d) for Fr = 3.2. The dashed lines indicate the typical values for background ocean turbulence, which serve as detection thresholds.

Particularly intriguing are the microstructure signatures, conventionally expressed in terms of turbulent and thermal dissipation rates. These quantities are often assumed to be proportional and, in the oceanographic literature, used interchangeably to identify and quantify small-scale turbulence in the ocean. The present configuration, on the other hand, is characterized by the dissimilar behavior of thermal and dynamic microstructure signatures. The turbulent dissipation rate (ε) exhibits very limited sensitivity to stratification, and its decay patterns are generally consistent with those predicted by Spedding (1997). However, the thermal dissipation rate (χ) varies substantially—by as much as an order of magnitude—with stratification. The identifiable thermal microstructure signal typically persists much longer than its ε-based counterpart.

TABLE II. Decay rates, maximum detection time, and drag coefficient.

	λ_χ	D_χ	$N_0 D_\chi$	λ_ε	D_ε	$N_0 D_\varepsilon$	c_d
EXP 1A	−1.70	380	380	−1.45	34	34	0.012
EXP 2A	−1.72	460	460	−1.67	29	29	0.012
EXP 3A	−1.03	>500	>500	−1.22	30	30	0.012
EXP 4A	−1.24	350	350	−2.03	27	27	0.012
EXP 1B	−2.67	126	42	−2.01	27	9.0	0.012
EXP 2B	−1.64	132	44	−1.82	23	7.8	0.013
EXP 3B	−1.97	420	140	−1.84	29	9.5	0.012
EXP 4B	−1.83	66	22	−2.02	21	9.2	0.011

The internal waves produced by the passage of the object also change with both ambient and local stratification. The wave activity in non-uniformly stratified systems is generally more intense. This result is consistent with prior analyses internal wave transmission, such as the simulations of Brucker and Sarkar (2010). In addition, at higher values of Fr (for a given Re), the internal waves produced by the body are less influenced by local changes in the stratification. This effect is attributed to the larger spatial extent of internal waves in high-Fr simulations (Meunier *et al.*, 2018), which impedes their reflection by local changes in stratification.

In summary, the evidence of wake sensitivity to localized changes in stratification is compelling. These findings promote future wake research in several directions. The analyses of dynamic ramifications

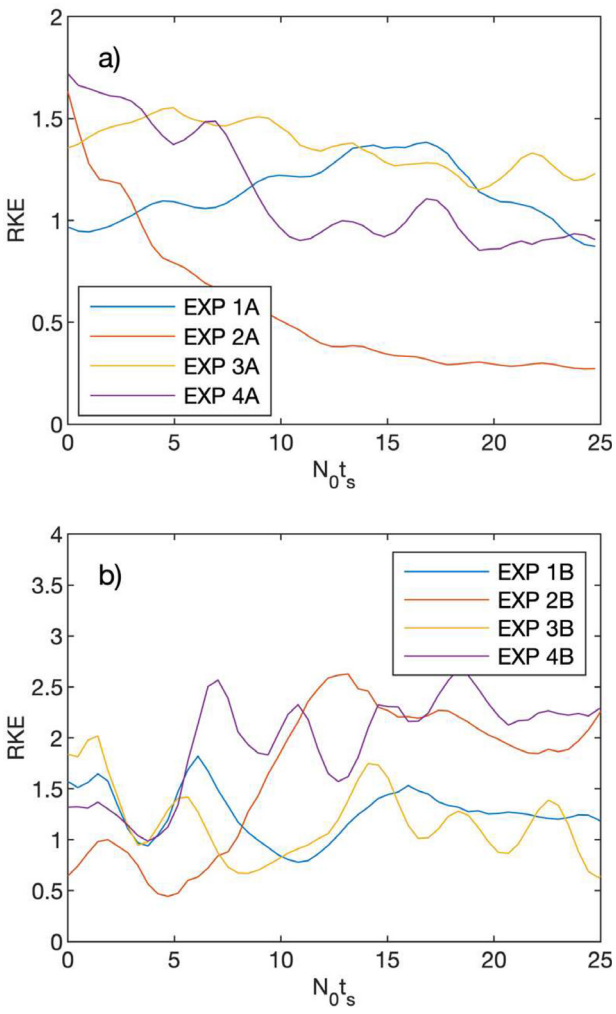

FIG. 11. Ratio of kinetic energy for (a) Fr = 1.0 and (b) Fr = 3.2.

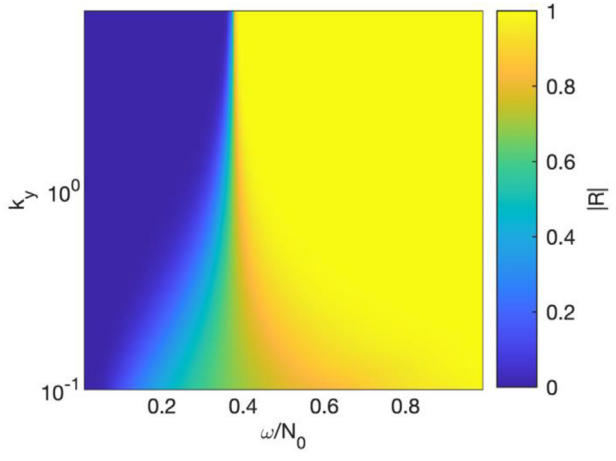

FIG. 12. Reflection coefficient. The reflectivity index is based on the relation between horizontal wavenumber, k_y, and ω/N_0 for EXP 2A.

of non-uniform stratification should be extended to laboratory and oceanographic experiments, where the spatial variability of density gradients occurs naturally. Particularly promising in this regard are the concurrent modeling and observational efforts that would combine the ground-truth of field measurements with the accessibility and dynamical transparency of simulations. Our results also underscore the need for more elaborate internal wave schemes that would extend the efforts described in Voisin (1994), Broutman *et al.* (2004), and Brucker and Sarkar (2010). Finally, we recommend the extension of the present analyses of intermediate wakes into the late stages, characterized by the emergence of coherent long-lived vortical structures. Based on our results, we anticipate that the late wake structure would also be highly sensitive to changes in the background stratification.

ACKNOWLEDGMENTS

This work used the Extreme Science and Engineering Discovery Environment (XSEDE), which is supported by National Science Foundation Grant No. ACI-1548562. Specifically, it used the Bridges-2 system, which is supported by NSF Award No. ACI-1928147, at the Pittsburgh Supercomputing Center (PSC). The authors also received support from the Office of Naval Research, Grant No. N0001420WX00354.

AUTHOR DECLARATIONS

Conflict of Interest

The authors have no conflicts to disclose.

Author Contributions

Elias Nadaf: Formal analysis (equal); Visualization (equal); Writing – original draft (equal); Writing – review & editing (equal). **Justin Michael Brown:** Methodology (equal); Software (equal); Supervision (equal); Writing – review & editing (equal). **Timour Radko:** Conceptualization (equal); Funding acquisition (equal); Project administration (equal); Supervision (equal); Writing – review & editing (equal).

DATA AVAILABILITY

The data that support the findings of this study are available from the corresponding author upon reasonable request.

APPENDIX A: THE ISOMORPHISM OF WAKES

We begin with the Boussinesq equations for a single-component fluid, decomposing the temperature according to $T_0 + T(t,x,y,z) + T_z z + \overline{T_1}(t,z)$, where T_0 and T_z are constant, $\overline{T_1}(t,z)$ is a predetermined initial deviation away from the uniform temperature gradient that can evolve in time, and T is the thermal perturbation. We similarly decompose the pressure into $p(t,x,y,z) + p_z z$,

$$\frac{\partial \mathbf{u}}{\partial t} + \mathbf{u}\cdot\nabla\mathbf{u} = -\frac{\nabla p}{\rho_0} + \alpha g\left(T + \overline{T_1}\right)\hat{\mathbf{k}} + \nu\nabla^2\mathbf{u}, \tag{A1}$$

$$\frac{\partial\left(T + \overline{T_1}\right)}{\partial t} + \mathbf{u}\cdot\nabla\left(T + \overline{T_1}\right) + wT_z = k_T\nabla^2\left(T + \overline{T_1}\right), \tag{A2}$$

$$\nabla\cdot\mathbf{u} = 0, \tag{A3}$$

where we have already removed hydrostatic balance [$\nabla p_z = \rho_0 \alpha g(T_0 + T_z z)$]. For this discussion, all quantities are dimensional, and the asterisks ordinarily uses to differentiate dimensional quantities are omitted. In the absence of motion, the thermal equation becomes

$$\frac{\partial \overline{T_1}}{\partial t} = k_T \nabla^2 (\overline{T_1}), \tag{A4}$$

which we can subtract from Eq. (A2) to yield

$$\frac{\partial \mathrm{T}}{\partial t} + \mathbf{u} \cdot \nabla T = -wT_z - w\frac{\partial \overline{T_1}}{\partial z} + k_T \nabla^2 T. \tag{A5}$$

We consider a (primed) system with $\overline{T_1}'(t,z) = -\overline{T_1}(t,-z)$. Assuming that u, v, w, p, and T are a solution for $\overline{T_1}(t,z)$, we will show that the following equations form a solution for $\overline{T_1}'(t,z)$:

$$u'(t,\, x,\, y,\, z) = u(t,\, x,\, y,\, -z), \tag{A6}$$

$$v'(t,\, x,\, y,\, z) = v(t,\, x,\, y,\, -z), \tag{A7}$$

$$w'(t,\, x,\, y,\, z) = -w(t,\, x,\, y,\, -z), \tag{A8}$$

$$p'(t,\, x,\, y,\, z) = p(t,\, x,\, y,\, -z), \tag{A9}$$

$$T'(t,\, x,\, y,\, z) = -T(t,\, x,\, y,\, -z). \tag{A10}$$

For the continuity equation, this would require

$$\nabla \cdot \mathbf{u}'(t,x,y,z) = \frac{\partial u(t,x,y,-z)}{\partial x} + \frac{\partial v(t,x,y,-z)}{\partial y} + \frac{\partial(-w(t,x,y,-z)}{\partial z} = 0. \tag{A11}$$

Under the transformation of $z' = -z$, this becomes

$$\frac{\partial u(t,x,y,z')}{\partial x} + \frac{\partial v(t,x,y,z')}{\partial y} - \frac{\partial(-w(t,x,y,z')}{\partial z'} = 0, \tag{A12}$$

which is equivalent to the original continuity equation with z' instead of z. From this point on, all discussion will be for variables in the (t,x,y,z') coordinate transformation and the coordinates will be dropped for convenience. We can treat the temperature equation in a similar way to the continuity equation, finding

$$-\frac{\partial T}{\partial t} + u\frac{\partial(-T)}{\partial x} + v\frac{\partial(-T)}{\partial y} - (-w)\frac{\partial(-T)}{\partial z'} = wT_z - w\frac{\partial(-\overline{T_1})}{\partial z'} - k_T \nabla'^2 T, \tag{A13}$$

where we have denoted $\nabla' \equiv (\partial/\partial \mathrm{x}, \partial/\partial \mathrm{y}, \partial/\partial z')$. Again, this is equivalent to the original temperature evolution equation. We note that converting the Laplacian to the primed coordinate system (∇'^2) does not cause a change of sign because

$$\left(-\frac{\partial}{\partial z'}\right)\left(-\frac{\partial}{\partial z'}\right) = \frac{\partial^2}{\partial z'^2}. \tag{A14}$$

The components of the momentum equation for the primed solution can be shown to be equivalent to the original equation components by the same method

$$\frac{\partial u}{\partial t} + u\frac{\partial u}{\partial x} + v\frac{\partial u}{\partial y} - (-w)\frac{\partial u}{\partial z'} = -\frac{1}{\rho_0}\frac{\partial p}{\partial x} + \nu \nabla'^2 u, \tag{A15}$$

$$\frac{\partial u}{\partial t} + u\frac{\partial u}{\partial x} + v\frac{\partial u}{\partial y} - (-w)\frac{\partial u}{\partial z'} = -\frac{1}{\rho_0}\frac{\partial p}{\partial y} + \nu \nabla'^2 v, \tag{A16}$$

$$-\frac{\partial w}{\partial t} + u\frac{\partial(-w)}{\partial x} + v\frac{\partial(-w)}{\partial y} - (-w)\frac{\partial(-w)}{\partial z'} = \frac{1}{\rho_0}\frac{\partial p}{\partial z'} + \alpha g(-T - \overline{T_1}) - \nu \nabla'^2 w. \tag{A17}$$

In summary, this shows that if a solution to the Boussinesq equations exists for an initial temperature field of $T_z \mathrm{z} + \overline{T_1}(0,z)$, then a mirrored system with initial condition $T_z \mathrm{z} - \overline{T_1}(0,-z)$ will have the same solution only mirrored around $\mathrm{z} = 0$ and with the thermal perturbation and vertical velocity of opposite sign.

APPENDIX B: INTERNAL WAVE TRANSMISSION

Given a buoyancy frequency profile, it is possible to determine the total reflection and transmission of incident internal waves. We use an idealized model for internal waves in two dimensions

$$\left(N^2(z) - \omega^2\right)\frac{\partial^2}{\partial y^2}\hat{\mathrm{w}} = \omega^2 \frac{\partial^2}{\partial z^2}\hat{w}, \tag{B1}$$

where $N(\mathrm{z})$ is the buoyancy frequency, which can change with depth, and $\hat{w}$ is the amplitude of the vertical velocity field, which oscillates at an angular frequency of ω, assumed constant. We assume solutions of the form

$$\hat{w} = A(z)e^{ik_y y}, \tag{B2}$$

where A is the z-dependent amplitude of the internal wave and k_y is the constant horizontal wavenumber. It is clear from these expressions that the solutions depend only on the ratio between N^2 and ω^2. Internal waves generated far from the disturbance at $z = 0$ will have angular frequencies in the range of $-N < \omega < N$. For internal waves to transmit, N^2/ω^2 must exceed unity on scales larger than $2\pi/\mathrm{k}_z$ or else any evanescent waves will be unable to penetrate the region. This serves to provide an upper bound on waves expected to transmit for a given expression of N^2. For a typical Gaussian perturbation,

$$T = z + \gamma \exp\left(-\frac{z^2}{\sigma^2}\right), \tag{B3}$$

$$N^2 = \mathrm{Fr}^{-2}\left(1 - \frac{2\gamma z}{\sigma^2}\exp\left(-\frac{z^2}{\sigma^2}\right)\right), \tag{B4}$$

we define an ambient buoyancy frequency of $N_0 = \mathrm{Fr}^{-1}$ in our non-dimensional system and can therefore represent the internal wave angular frequency as $\omega = N_0 \cos\theta$, where θ can be shown to be the angle of wave propagation from the horizontal axis. This results in an expression for their ratio given by

$$\frac{N^2}{\omega^2} = \frac{N^2}{N_0^2 \cos^2\theta} = \frac{1}{\cos^2\theta} - \frac{2\gamma z}{\sigma^2 \cos^2\theta}\exp\left(-\frac{z^2}{\sigma^2}\right), \tag{B5}$$

and this limits the range of θ that can be transmitted to

$$\sin^2\theta > \frac{2\gamma}{\sigma}\max\left(2z'\exp\left(-z'^2\right)\right). \tag{B6}$$

The maximum of $2\hat{z}e^{-\hat{z}^2}$ is a constant that must be found numerically.

To determine the transmission coefficient, we numerically integrate the amplitude of the internal wave from a distant point in $-z\,(-10\sigma)$ to a distant point in $+z\,(10\sigma)$ given an initial value of A and A', the z-derivative of A. We consider that the wave amplitude at the start, $A(-10\sigma)$, is the sum of the incident (assumed to have an amplitude of unity) and reflected waves (with an amplitude of R), and the wave amplitude at the end, $A(10\sigma)$, is the amplitude of the transmitted wave (with an amplitude of Y). This means that the initial form of A would be well approximated by

$$A(z) = e^{ik_z z} + Re^{-ik_z z}, \tag{B7}$$

and the final form by

$$A(z) = Ye^{ik_z z}. \tag{B8}$$

However, it is difficult to ascertain *a priori* the correct complex value of R such that the transmitted wave contains no $e^{-ik_z z}$ component. Thus, we evolve two independent waves with initial values of A and A' given by $A = e^{\pm ik_z z}$, and yielding two final values (and derivatives) of A, which we denote as $A_\pm$ (and $A'_\pm$). To determine the correct value of R, we can construct a linear combination of A_- and A_+ such that Eq. (B8) holds true. Each result of the numerical integration yields a final value of A, which can be expressed in terms of the forward and backward propagating solutions:

$$A_\pm(z) = F_\pm e^{ik_z z} + B_\pm e^{-ik_z z}, \tag{B9}$$

and the amplitude of the backward propagating solution is then calculated from

$$B_\pm = e^{ik_z z}\left(A_\pm - \frac{1}{ik_z}A'_\pm\right). \tag{B10}$$

For this to be a valid solution, then the final state is given by

$$A(z) = F_+ e^{ik_z z} + B_+ e^{-ik_z z} + RF_- e^{ik_z z} + RB_- e^{-ik_z z}, \tag{B11}$$

where we require $B_+ + RB_- = 0$, so that there is no backward-propagating solution in the transmission region. The magnitude of the reflection coefficient is then simply

$$|R| = \frac{|B_+|}{|B_-|}. \tag{B12}$$

REFERENCES

Abdilghanie, A. and Diamessis, P., "The internal gravity wave field emitted by a stably stratified turbulent wake," J. Fluid Mech. **720**, 104–139 (2013).

Bonnier, M. and Eiff, O., "Experimental investigation of the collapse of a turbulent wake in a stably stratified fluid," Phys Fluids **14**, 791 (2002).

Broutman, D., Rottman, J., and Eckerman, S., "Ray methods for internal waves in the atmosphere and ocean," Annu. Rev. Fluid Mech. **36**, 233–253 (2004).

Brucker, K. and Sarkar, S., "A comparative study of self-propelled and towed wakes in a stratified fluid," J. Fluid Mech. **652**, 373–404 (2010).

Chongsiripinyo, K., Pal, A., and Sarkar, S., "On the vortex dynamics of flow past a sphere at Re = 3700 in a uniformly stratified fluid," Phys Fluids **29**, 020704 (2017).

De Stadler, M., "High resolution simulation of the turbulent wake behind a sphere in a stratified fluid," Ph.D. dissertation (Department of Engineering Science, UC San Diego, 2013).

Diamessis, P. J., Spedding, G. R., and Domaradzki, J. A., "Similarity scaling and vorticity structure in high-Reynolds-number stably stratified turbulent wakes," J. Fluid Mech. **671**, 52–95 (2011).

Gilreath, H. E. and Brandtt, A., "Experiments on the generation of internal waves in a stratified fluid," AIAA J. **23**, 693–700 (1985).

Gregg, M. C., D'Asaro, E. A., Riley, J. J., and Kunze, E., "Mixing efficiency in the ocean," Annu. Rev. Mar. Sci. **10**, 443–473 (2018).

Gourlay, M. J., Arendt, S. C., Fritts, D. C., and Werne, J., "Numerical modeling of initially turbulent wakes with net momentum," Phys. Fluids **13**, 3783–3802 (2001).

Holzmann, T., *Mathematics, Numerics, Derivations and OpenFOAM®, Release 7.0* (Holzmann CFD, 2019).

Hopfinger, E. J., Flor, J. B., Chomaz, J. M., and Bonneton, P., "Internal waves generated by a moving sphere and its wake in a stratified fluid," Exp. Fluids **11**, 255–261 (1991).

Kaminski, A. K. and Smyth, W. D., "Stratified shear instability in a field of pre-existing turbulence," J. Fluid Mech. **862**, 639–658 (2019).

Katija, K., "Biogenic inputs to ocean mixing," J. Exp. Biol. **215**(6), 1040–1049 (2012).

Keller, J. B. and Munk, W. H., "Internal wave wakes of a body moving in a stratified fluid," Phys. Fluids **13**, 1425 (1970).

Lewin, S. F. and Caulfield, C. P., "The influence of far field stratification on shear-induced turbulent mixing," J. Fluid Mech. **928**, A20 (2021).

Lin, Q., Boyer, D. L., and Fernando, H. J. S., "Turbulent wakes of linearly stratified flow past a sphere," Phys. Fluids A **4**, 1687–1696 (1992).

Lin, J. T. and Pao, Y. H., "Wakes in stratified fluids," Annu. Rev. Fluid Mech. **11**, 317–338 (1979).

Meunier, P., Diamessis, P. J., and Spedding, G. R., "Self-preservation in stratified momentum wakes," Phys. Fluids **18**, 106601 (2006).

Meunier, P., Le Dizès, S., Redekopp, L., and Spedding, G. R., "Internal waves generated by a stratified wake: Experiment and theory," J. Fluid Mech. **846**, 752–788 (2018).

Meunier, P. and Spedding, G. R., "A loss of memory in stratified momentum wakes," Phys. Fluids **16**, 298–305 (2004).

Miersch, L., Hanke, W., Wieskotten, S., Hanke, F. D., Oeffner, J., Leder, A., Brede, M., Witte, M., and Dehnhardt, G., "Flow sensing by pinniped whiskers," Philos. Trans. R. Soc. B **366**, 3077–3084 (2011).

Moody, Z., Merriam, C., Radko, T., and Joseph, J., "On the structure of stratified wakes generated by submerged propagating objects," J. Oper. Oceanogr. **10**, 191–204 (2017).

Negretti, M. E., Vignoli, G., Tubino, M., and Brocchini, M., "On shallow-water wakes: An analytical study," J. Fluid Mech. **567**, 457–475 (2006).

Pham, H. T., Sarkar, S., and Brucker, K. A., "Dynamics of a stratified shear layer above a region of uniform stratification," J. Fluid Mech. **630**, 191–223 (2009).

Pal, A., Sarkar, S., Posa, A., and Balaras, E., "Direct numerical simulation of stratified flow past a sphere at a subcritical Reynolds number of 3700 and moderate Froude number," J. Fluid Mech. **826**, 5–31 (2017).

Pao, Y. H., "Measurements of internal waves and turbulence in two-dimensional stratified shear flows," Boundary-Layer Meteorol. **5**, 177–193 (1973).

Pao, H. P., Robert, Y. L., and Charles, E. S., "Vortex trails in stratified fluids," Johns Hopkins APL Tech. Dig. **3**, 12–18 (1982).

Radko, T. and Lorfeld, D., "Effects of weak planetary rotation on the stability and dynamics of internal stratified jets," Phys. Fluids **30**, 096602 (2018).

Radko, T. and Lewis, D., "The age of a wake," Phys. Fluids **31**, 076601 (2019).

Redford, J. A., Lund, T. S., and Coleman, G. N., "A numerical study of a weakly stratified turbulent wake," J. Fluid Mech. **776**, 568–609 (2015).

Rottman, J. W., Broutman, D., Spedding, G., and Meunier, P., "The internal wave field generated by the body and wake of a horizontally moving sphere in a stratified fluid," in Proceedings of the 15th Australasian Fluid Mechanics Conference, Sydney, Australia, 2004.

Rowe, K. L., Diamessis, P. J., and Zhou, Q., "Internal gravity wave radiation from a stratified turbulent wake," J. Fluid Mech. **888**, A25 (2020).

Schooley, A. H. and Stewart, R. W., "Experiments with a self-propelled body submerged in a fluid with vertical density gradient," J. Fluid Mech. **15**, 83–99 (1963).

Snyder, M., Kang, H., and Burks, J., "Validation of computational ship air wakes for a naval research vessel," in *51st AIAA Aerospace Sciences Meeting Including the New Horizons Forum and Aerospace Exposition* (AIAA, 2013).

Spedding, G. R., "The evolution of initially turbulent bluff-body wakes at high internal Froude number," J. Fluid Mech. **337**, 283–301 (1997).

Spedding, G. R., "Wake signature detection," Annu. Rev. Fluid Mech. **46**, 273–302 (2014).
Spedding, G. R., Browand, F., and Fincham, A. M., "The long-time evolution of the initially turbulent wake of a sphere in a stable stratification," Dyn. Atmos. Oceans **23**, 171–182 (1996).
Sutyrin, G. G. and Radko, T., "The fate of pancake vortices," Phys. Fluids **29**, 031701 (2017).
Switzer, G. F. and Proctor, F. H., "Numerical study of wake vortex behavior in turbulent domains with ambient stratification," in *38th Aerospace Sciences Meeting & Exhibit, Reno, NV* (AIAA, 2000).
Tisovska, P., "Description of the overset mesh approach in ESI version of OpenFOAM," in Proceedings of CFD with OpenSource Software, 2019.
Watanabe, T., Riley, J. J., Nagata, K., Onishi, R., and Matsuda, K., "A localized turbulent mixing layer in a uniformly stratified environment," J. Fluid Mech. **849**, 245–276 (2018).
Waterhouse, A. F., MacKinnon, J. A., Nash, J. D., Alford, M. H., Kunze, E., Simmons, H. L., Polzin, K. L., St. Laurent, L. C., Sun, O. M., Pinkel, R., Talley, L. D., Whalen, C. B., Huussen, T. N., Carter, G. S., Fer, I., Waterman, S., Naveira Garabato, A. C., Sanford, T. B., and Lee, C. M., "Global patterns of diapycnal mixing from measurements of the turbulent dissipation rate," J. Phys. Oceanogr. **44**(7), 1854–1872 (2014).
Weller, H. G., Tabor, G., Jasak, H., and Furebym, C., "A tensorial approach to computational continuum mechanics using object-oriented techniques," Comput. Phys. **12**, 620 (1998).
Wieskotten, S., Dehnhardt, G., Mauck, B., Miersch, L., and Hanke, W., "The impact of glide phases on the trackability of hydrodynamic trails in harbour seals (*Phoca vitulina*)," J. Exp. Biol. **213**(21), 3734–3740 (2010).
VanDine, A., Pham, H. T., and Sarkar, S., "Turbulent shear layers in a uniformly stratified background: DNS at high Reynolds number," J. Fluid Mech. **916**, A42 (2021).
Voisin, B., "Internal wave generation in uniformly stratified fluids. Part 2. Moving point sources," J. Fluid Mech. **261**, 333–374 (1994).
Voropayev, S. I., Fernando, H. J. S., Smirnov, S. A., and Morrison, R., "On surface signatures generated by submerged momentum sources," Phys. Fluids **19**, 076603 (2007).
Zhou, Q. and Diamessis, P., "Surface manifestation of internal waves emitted by submerged localized stratified turbulence," J. Fluid Mech. **798**, 505–539 (2016).